Journal of Colloid and Interface Science **234,** 204–216 (2001)
doi:10.1006/jcis.2000.7295, available online at http://www.idealibrary.com on IDEAL®

Mechanisms of Arsenic Adsorption on Amorphous Oxides Evaluated Using Macroscopic Measurements, Vibrational Spectroscopy, and Surface Complexation Modeling

Sabine Goldberg*,[1] and Cliff T. Johnston†

*George E. Brown, Jr. Salinity Laboratory, Riverside, California 92507; and †Purdue University, West Lafayette, Indiana 47907

Received June 26, 2000; accepted October 16, 2000

Arsenic adsorption on amorphous aluminum and iron oxides was investigated as a function of solution pH, solution ionic strength, and redox state. In this study *in situ* Raman and Fourier transform infrared (FTIR) spectroscopic methods were combined with sorption techniques, electrophoretic mobility measurements, and surface complexation modeling to study the interaction of As(III) and As(V) with amorphous oxide surfaces. The speciation of As(III) and As(V) in aqueous solution was examined using Raman and attenuated total reflectance (ATR)-FTIR methods as a function of solution pH. The position of the As–O stretching bands, for both As(III) and As(V), are strongly pH dependent. Assignment of the observed As–O bands and their shift in position with pH was confirmed using semiempirical molecular orbital calculations. Similar pH-dependent frequency shifts are observed in the vibrational bands of As species sorbed on amorphous Al and Fe oxides. The mechanisms of As sorption to these surfaces based on the spectroscopic, sorption, and electrophoretic mobility measurements are as follows: arsenate forms inner-sphere surface complexes on both amorphous Al and Fe oxide while arsenite forms both inner- and outer-sphere surface complexes on amorphous Fe oxide and outer-sphere surface complexes on amorphous Al oxide. These surface configurations were used to constrain the input parameters of the surface complexation models. Inclusion of microscopic and macroscopic experimental results is a powerful technique that maximizes chemical significance of the modeling approach.

Key Words: **arsenate; arsenite; amorphous aluminum oxide; amorphous iron oxide; FTIR spectroscopy; Raman spectroscopy.**

INTRODUCTION

Arsenic is a trace element that is toxic to animals including humans. Concentrations of As in soils and waters can become elevated due to mineral dissolution, use of arsenical pesticides, disposal of fly ash, mine drainage, and geothermal discharge. At present, there is widespread concern about elevated concentrations of As in the aquifers of Bangladesh. Of the 125 million people living in Bangladesh the number adversely affected by As-contaminated drinking water has been estimated to be between 50 and 70 million. The elevated concentrations of As have been attributed to pyritic sedimentary rocks in contact with the aquifer. There is no general consensus, however, about what mechanisms are responsible for the increased concentration of As in the groundwater. Conflicting mechanisms have been invoked including arguments based on oxidation and reduction. In addition, elevated concentrations of As are found in agricultural drainage waters from some soils in arid regions.

Of the two naturally occurring forms of As, arsenate, As(V), and arsenite, As(III), the As(III) redox state is considerably more toxic. Current Federal water quality standards indicate that As concentrations in excess of 50 ppb are hazardous to the welfare of humans and domestic animals. At natural pH values arsenite exists in solution only as H_3AsO_3 and $H_2AsO_3^-$ since the pK_a values are high: p$K_a^1 = 9.2$ and p$K_a^2 = 12.7$. Arsenate can exist in solution as H_3AsO_4, $H_2AsO_4^-$, $HAsO_4^{2-}$, and AsO_4^{3-} with p$K_a^1 = 2.3$, p$K_a^2 = 6.8$, and p$K_a^3 = 11.6$. Because the kinetics of As redox transformations are relatively slow, both oxidation states are often found in soil and subsurface environments regardless of the redox condition (1). Sorption studies of arsenite and arsenate have used a wide range of sorbents including iron and aluminum oxides, phyllosilicates, soil organic matter, and whole soils. Both arsenite and arsenate show high affinity for Fe oxides in soil and subsurface environments. In fact, Fe oxides have been implicated as a controlling solid phase in Bangladeshi geologic materials. The As that is associated with the pyritic sandstones is thought to be associated with Fe oxides. Under reducing conditions the solubility of these As-containing solid phases is increased and is responsible, in part, for the elevated concentrations in the water supply (2).

Both arsenite and arsenate are adsorbed on soil mineral surfaces but have very different adsorption behaviors. In general terms, arsenate sorption on amorphous Al and Fe oxides is characterized by an apparent sorption maximum at a pH value of 4 (3–5). In contrast, arsenite adsorption is characterized by a sorption maximum occurring in the pH range of 7 to 8.5 (4, 6). Ionic strength effects are more apparent in arsenite sorption studies and it is generally held that arsenate is more strongly bound than arsenite.

[1] To whom correspondence should be addressed at USDA-ARS, George E. Brown, Jr. Salinity Laboratory, 450 W. Big Springs Road, Riverside, CA 92507.

0021-9797/01 $35.00

Studies of As adsorption on amorphous oxides have concentrated on the Fe oxide ferrihydrite (4, 5, 7–14). Direct experimental observation of the mechanisms of ion attachment on surfaces can be carried out using spectroscopic techniques. For applicability to natural systems, spectroscopic methods must be capable of evaluating surface-adsorbed ions in the presence of water. Fourier transform infrared (FTIR), extended X-ray absorption fine structure (EXAFS), and Raman spectroscopies are all capable of examining adsorption in aqueous conditions. Arsenate adsorbs on ferrihydrite as inner-sphere surface complexes that are attached predominantly via bidentate linkages with some monodentate linkages (8). Results of FTIR analyses in conjunction with point of zero charge shifts and titration data suggest monodentate attachment of $H_2AsO_4^-$ on amorphous Fe oxide and monodentate attachment of $H_2AsO_3^-$ on amorphous Fe and Al oxides (15). The As(III)/As(V)–goethite system has been the subject of several spectroscopic investigations. Extended X-ray absorption fine structure spectra of arsenate sorbed on goethite (FeOOH) have revealed three different inner-sphere As(V)–goethite complexes characterized by As–Fe distances of 0.285, 0.323, and 0.360 nm, respectively (16). Similarly, X-ray absorption spectra (XAS) of the As(III)–goethite complex were characterized by a well-resolved As–Fe distance of 0.338 nm corresponding to a binuclear inner-sphere complex showing little pH or concentration dependence at surface coverages ranging from 1.9 to 4.3 μmol m^{-2} (17). Although the sorption of arsenite and arsenate on goethite is very different, the XAS data reveal similar surface complexes that show little pH or surface coverage dependence.

Descriptions of As adsorption behavior in natural systems require knowledge of the mode of bonding of the As anions on mineral surfaces. Macroscopic and microscopic experimental methods can both provide insight into anion adsorption mechanisms. Electrophoretic mobility, EM, is a measure of the movement of charged particles in response to an applied electric field. Zero EM indicates the condition of zero surface charge called the point of zero charge (PZC). Shifts in PZC of minerals and reversals of EM with increasing ion concentration can be used as evidence of strong specific ion adsorption and inner-sphere surface complex formation. Inner-sphere surface complexes contain no water molecules between the adsorbing ion and the surface functional group; outer-sphere surface complexes contain one or more water molecules between the surface functional group and the adsorbing ion. If the assumption is made that outer-sphere complexes lie outside the shear plane, then electrophoresis may be used to distinguish inner- and outer-sphere surface complexes. Shifts in PZC have been observed following arsenate (5, 15) and arsenite adsorption on amorphous Fe oxide (7, 15) and arsenate adsorption on amorphous Al oxide (3).

Evaluation of the effect of changes in ionic strength on adsorption behavior is another macroscopic method of inferring adsorption mechanisms. McBride (18) indicates that ions that form outer-sphere surface complexes show decreasing adsorption with increasing solution ionic strength. Ions that form inner-sphere surface complexes show little ionic strength dependence or show increasing adsorption with increasing solution ionic strength. Greater ion adsorption with increasing ionic strength is due to the higher activity of the counter ions in solution available to compensate the surface charge generated by specific ion adsorption. Arsenate adsorption on amorphous Fe oxide (5) and arsenite adsorption on amorphous Al oxide (6) showed very little ionic strength dependence as a function of solution pH, suggesting an inner-sphere adsorption mechanism.

Surface complexation models are chemical models that have been used to describe ion adsorption on oxide minerals. The constant capacitance model was able to describe arsenate and arsenite adsorption on amorphous Al oxide (6, 19). Arsenate and arsenite adsorption on amorphous Fe oxide were described by the generalized two-layer model (20). Hering *et al.* (11) used surface complexation constants determined by Dzombak and Morel (20) to predict arsenate and arsenite removal during coagulation with ferric chloride. The triple-layer model was used to describe arsenate adsorption on amorphous Fe oxide (10).

Our study focuses on As adsorption on amorphous Fe and Al oxides that unlike crystalline oxides such as goethite, have not been thoroughly characterized yet. These materials constitute a major ion-adsorbing sink in soils. A combination of macroscopic and microscopic techniques is appropriate to delineate the adsorption mechanisms of arsenate and arsenite. Our study contains the following objectives: (i) to determine arsenate and arsenite adsorption on amorphous Al and Fe oxide as a function of solution pH and ionic strength; (ii) to determine PZCs of amorphous Fe and Al oxide with and without arsenate or arsenite; (iii) to evaluate the ability of surface complexation models to describe arsenate and arsenite adsorption on these surfaces; (iv) to investigate adsorbed As on amorphous oxides using Raman and FTIR spectroscopies. In our study we combine macroscopic and microscopic techniques for evaluating adsorption mechanisms. The results are used to constrain the input parameters of the surface complexation models and thus maximize the chemical significance of the model applications.

MATERIALS AND METHODS

Macroscopic Experimental Methods

Arsenic adsorption behavior as a function of solution pH and ionic strength was studied on amorphous oxides. Amorphous Al and Fe oxides were synthesized as described by Sims and Bingham (21). For the amorphous Al oxide synthesis, the $AlCl_3$ was neutralized with an equal part of 4.0 M NaOH. X-ray diffraction analyses were used to verify that the oxides were amorphous and contained no trace impurities. Surface areas were determined with a single-point BET N_2 adsorption isotherm obtained using a Quantasorb Jr. surface area analyzer. The surface area of the Fe oxide was 290 m^2/g and the surface area of the Al oxide was 209 m^2/g.

Points of zero charge and EMs for the oxides were determined by microelectrophoresis using a Zeta-Meter 3.0 system. The EMs of oxide suspensions containing 0.02% solid in 0.01 M NaCl were determined at various pH values. The PZCs were obtained by interpolating the data to zero EM. Electrophoretic mobility measurements were also determined in the presence of 0.01 or 1.0 mM As(III) or As(V).

Arsenic adsorption experiments were carried out in batch systems to determine adsorption envelopes (amount of As adsorbed as a function of solution pH per fixed total As concentration). Samples of adsorbent were added to 50-ml polypropylene centrifuge tubes or 250-ml centrifuge bottles and equilibrated with aliquots of a 0.01, 0.1, or 1.0 M NaCl solution by shaking for 4 h on a reciprocating shaker at $22.6 \pm 0.5^{\circ}$C. Solid suspension density of oxide was 0.5 or 4.0 g L^{-1}. The equilibrating solutions contained 0.1 or 1.0 mM As from $Na_2HAsO_4 \cdot 7H_2O$ or $NaAsO_2$ and were adjusted to the desired pH values using 1.0 M HCl or NaOH additions that changed the total volume by $\leq$2%. The pH was measured using a Corning Ion Analyzer 150 with a research grade combination standard Ag–AgCl reference electrode with a ceramic plug liquid junction manufactured by Thomas Scientific. The electrode was calibrated using a pH 4 potassium biphthalate buffer and a pH 6.86 sodium and potassium phosphate buffer. The samples were centrifuged at a relative centrifugal force of 7800*g* for 20 min. The decantates were analyzed for pH, filtered through a 0.45-μm Whatman filter, and analyzed for As concentration using inductively coupled plasma (ICP) emission spectrometry.

Samples for spectroscopic analysis were prepared by reacting 2.0 g of oxide with 12.5 ml of a 0.1 M NaCl solution containing 0.1 M As(III) at pH 5 or pH 10.5 or As(V) at pH 5 or pH 9. Samples were used wet or rinsed with 20 ml of doubly deionized water and air-dried. Reference samples were reacted with a solution containing only 0.1 M NaCl.

Raman Spectroscopy

Polarized Raman spectra were obtained on an Acton Research Corporation SpectroPro500 spectrograph. A Melles-Griot helium–neon laser with 632.8-nm wavelength and power output of 40 mW measured at the laser head was used as the excitation source. Raman-scattered radiation was collected in a 180° backscattering configuration and a polarization analyzer was used to select the polarization of the Raman-scattered light along either the *X* or the *Y* axis. A calcite-wedge polarization scrambler was placed after the analyzer to minimize unwanted polarization effects in the spectrograph. The polarization discrimination of the instrument was checked by measuring the depolarization ratio for the 459 cm^{-1} band of CCl_4. The experimental value was 0.023 compared to a theoretical value of 0.01 (22). The entrance slits to the spectrograph were set to 100 μm, which corresponded to a resolution of 5 cm^{-1}. The spectrograph used a holographic grating with 1200 grooves per millimeter with a blaze wavelength of 532 nm. The detector was a Princeton Instruments liquid N_2 cooled CCD detector with an active array of 1100 (h) $\times$ 330 (v) pixels. The spectrograph was calibrated daily using a Ne–Ar calibration lamp based upon known spectral lines. Spectra were typically collected using 300 s of acquisition on the CCD array. The Grams-386 program from Galactic Software was used to analyze and plot the Raman and IR spectra. Raman spectra of As(III) and As(V) solutions were collected from 0.1 M solutions in 6-mm NMR tubes using a 180° backscattering geometry through an Olympus BX-60 microscope using a 50X objective. Raman spectra of As(V) sorbed to Al oxide were also collected from a 16 wt% suspension of the oxide in 6-mm NMR tubes.

FTIR Spectroscopy

FTIR spectra were obtained with a Perkin–Elmer Model 1800 spectrometer and a horizontal ATR attachment (Squareco) using a trapezoidal-shaped ZnSe internal reflection element with nine reflections at a 45° angle. The measured pathlength was 20 μm at 1630 cm^{-1} based on the molar absorptivity of water. The ZnSe internal reflection element did not permit observation of IR bands below 750 cm^{-1}. Spectra were obtained at a resolution of 4 cm^{-1} with each spectrum corresponding to the coaddition of 128 scans using a medium-band liquid N_2 cooled MCT detector. IR spectra of arsenate and arsenite sorbed on Fe and Al oxides were obtained as dry samples in KBr pellets corresponding to 3 mg of sample in approximately 250 mg of spectral grade KBr.

Constant Capacitance Modeling

The constant capacitance model (23) was used to describe arsenate and arsenite adsorption behavior on the oxides as a function of solution pH. The computer program FITEQL, Version 3.1 (24), was used to fit intrinsic As surface complexation constants to the experimental adsorption data. In the constant capacitance model, the surface complexation reactions for the surface functional group *X*OH (where *X*OH represents a reactive surface hydroxyl bound to a metal ion, *X* (Al or Fe), in the oxide mineral) are defined by Eqs. [1]–[7] in Table 1. The constant capacitance model assumes that all surface complexes are inner-sphere. The intrinsic equilibrium constants for the inner-sphere surface complexation reactions of the surface functional group are given by Eqs. [8]–[14] in Table 1. The mass balance expression for the surface functional group is given by Eq. [15] or Eq. [16] and the charge balance expression is defined by Eq. [17] or Eq. [18] in Table 1. The relationship between surface charge and surface potential is Eq. [19] in Table 1.

In our application of the constant capacitance model, the surface site density was set at a value of 2.31 sites nm^{-2}, as recommended by Davis and Kent (25) for natural materials. Numerical values of the intrinsic protonation constant, K_+(int), and the intrinsic dissociation constant, K_-(int), were averages of a literature compilation of experimental values for Al and Fe oxides (26). The intrinsic protonation–dissociation constants were fixed at $\log K_+(\text{int}) = 7.31$ and $\log K_-(\text{int}) = -8.80$ for amorphous Fe oxide and $\log K_+(\text{int}) = 7.38$ and $\log K_-(\text{int}) = -9.09$ for amorphous Al oxide. A previous sensitivity analysis found that

TABLE 1
Equations and Reactions Used in the Constant Capacitance and Triple-Layer Models

Constant capacitance model	Triple-layer model (includes Eqs. [1]–[14] as for the constant capacitance model)
Surface complexation reactions	
$XOH_{(s)} + H^+_{(aq)} \rightleftarrows XOH^+_{2(s)}$ [1]	$XOH_{(s)} + Na^+_{(aq)} \rightleftarrows XO^-\text{–}Na^+_{(s)} + H^+_{(aq)}$ [20]
$XOH_{(s)} \rightleftarrows XO^-_{(s)} + H^+_{(aq)}$ [2]	$XOH_{(s)} + H^+_{(aq)} + Cl^-_{(aq)} \rightleftarrows XOH^+_2\text{–}Cl^-_{(s)}$ [21]
$XOH_{(s)} + H_3AsO_{4(aq)} \rightleftarrows XH_2AsO_{4(s)} + H_2O$ [3]	$XOH_{(s)} + H_3AsO_{4(aq)} \rightleftarrows XOH^+_2\text{–}H_2AsO^-_{4(s)}$ [22]
$XOH_{(s)} + H_3AsO_{4(aq)} \rightleftarrows XHAsO^-_{4(s)} + H^+_{(aq)} + H_2O$ [4]	$XOH_{(s)} + H_3AsO_{4(aq)} \rightleftarrows XOH^+_2\text{–}HAsO^{2-}_{4(s)} + H^+_{(aq)}$ [23]
$XOH_{(s)} + H_3AsO_{4(aq)} \rightleftarrows XAsO^{2-}_{4(s)} + 2H^+_{(aq)} + H_2O$ [5]	$XOH_{(s)} + H_3AsO_{4(aq)} \rightleftarrows XOH^+_2\text{–}AsO^{3-}_{4(s)} + 2H^+_{(aq)}$ [24]
$XOH_{(s)} + H_3AsO_{3(aq)} \rightleftarrows XH_2AsO_{3(s)} + H_2O$ [6]	$XOH_{(s)} + H_3AsO_{3(aq)} \rightleftarrows XOH^+_2\text{–}H_2AsO^-_{3(s)}$ [25]
$XOH_{(s)} + H_3AsO_{3(aq)} \rightleftarrows XHAsO^-_{3(s)} + H^+_{(aq)} + H_2O$ [7]	$XOH_{(s)} + H_3AsO_{3(aq)} \rightleftarrows XOH^+_2\text{–}HAsO^{2-}_{3(s)} + H^+_{(aq)}$ [26]
	$2XOH_{(s)} + H_3AsO_{3(aq)} \rightleftarrows (XOH^+_2)_2\text{–}HAsO^{2-}_{3(aq)}$ [27]
	$2XOH_{(s)} + H_3AsO_{3(aq)} \rightleftarrows (XOH^+_2)_2\text{–}AsO^{3-}_{3(aq)} + H^+_{(aq)}$ [28]
Surface complexation constants	
$K_+(\text{int}) = \frac{[XOH^+_2]}{[XOH][H^+]} \exp(F\psi_o/RT)$ [8]	$K_{Na^+}(\text{int}) = \frac{[XO^-\text{–}Na^+][H^+]}{[XOH][Na^+]} \exp[F(\psi_\beta - \psi_o)/RT]$ [29]
$K_-(\text{int}) = \frac{[XO^-][H^+]}{[XOH]} \exp(-F\psi_o/RT)$ [9]	$K_{Cl^-}(\text{int}) = \frac{[XSOH^+_2\text{–}Cl^-]}{[XOH][H^+][Cl^-]} \exp[F(\psi_o - \psi_\beta)/RT]$ [30]
$K^{1is}_{As(V)}(\text{int}) = \frac{[XH_2AsO_4]}{[XOH][H_3AsO_4]}$ [10]	$K^{1os}_{As(V)}(\text{int}) = \frac{[XOH^+_2\text{–}H_2AsO^-_4]}{[XOH][H_3AsO_4]} \exp[F(\psi_o - \psi_\beta)/RT]$ [31]
$K^{2is}_{As(V)}(\text{int}) = \frac{[XHAsO^-_4][H^+]}{[XOH][H_3AsO_4]} \exp(-F\psi_o/RT)$ [11]	$K^{2os}_{As(V)}(\text{int}) = \frac{[XOH^+_2\text{–}HAsO^{2-}_4][H^+]}{[XOH][H_2AsO_4]} \exp[F(\psi_o - 2\psi_\beta)/RT]$ [32]
$K^{3is}_{As(V)}(\text{int}) = \frac{[XAsO^{2-}_4][H^+]^2}{[XOH][H_3AsO_4]} \exp(-2F\psi_o/RT)$ [12]	$K^{3os}_{As(V)}(\text{int}) = \frac{[XOH^+_2\text{–}AsO^{3-}_4][H^+]^2}{[XOH][H_2AsO_4]} \exp[F(\psi_o - 3\psi_\beta)/RT]$ [33]
$K^{1is}_{As(III)}(\text{int}) = \frac{[XH_2AsO_3]}{[XOH][H_3AsO_3]}$ [13]	$K^{1os}_{As(III)}(\text{int}) = \frac{[XOH^+_2\text{–}H_2AsO^-_3]}{[XOH][H_3AsO_3]} \exp[F(\psi_o - \psi_\beta)/RT]$ [34]
$K^{2is}_{As(III)}(\text{int}) = \frac{[XHAsO^-_3][H^+]}{[XOH][H_3AsO_3]} \exp(-F\psi_o/RT)$ [14]	$K^{2os}_{As(III)}(\text{int}) = \frac{[XOH^+_2\text{–}HAsO^{2-}_3][H^+]}{[XOH][H_2AsO_3]} \exp[F(\psi_o - 2\psi_\beta)/RT]$ [35]
	$K^{1os}_{As(III)}(\text{int}) = \frac{[(XOH^+_2)\text{–}HAsO^{2-}_3]}{[XOH]^2[H_3AsO_3]} \exp[F(2\psi_o - 2\psi_\beta)/RT]$ [36]
	$K^{2os}_{As(III)}(\text{int}) = \frac{[(XOH^+_2)\text{–}AsO^{3-}_3][H^+]}{[XOH]^2[H_3AsO_3]} \exp[F(2\psi_o - 3\psi_\beta)/RT]$ [37]
Mass balances	
$[XOH]_T = [XOH] + [XOH^+_2] + [XO^-] + [XH_2AsO_4] + [XHAsO^-_4] + [XAsO^{2-}_4]$ [15]	$[XOH]_T = [XOH] + [XOH^+_2] + [XO^-] + [XH_2AsO_4] + [XHAsO^-_4] + [XAsO^{2-}_4] + [XOH^+_2\text{–}H_2AsO^-_4] + [XOH^+_2\text{–}HAsO^{2-}_4] + [XOH^+_2\text{–}AsO^{3-}_4] + [XO^-\text{–}Na^+] + [XOH^+_2\text{–}Cl^-]$ [38]
$[XOH]_T = [XOH] + [XOH^+_2] + [XO^-] + [XH_2AsO_3] + [XHAsO^-_3]$ [16]	$[XOH]_T = [XOH] + [XOH^+_2] + [XO^-] + [XH_2AsO_3] + [XHAsO^-_3] + [XOH^+_2\text{–}H_2AsO^-_3] + [XOH^+_2\text{–}HAsO^{2-}_3] + [XO^-\text{–}Na^+] + [XOH^+_2\text{–}Cl^-]$ [39]
Charge balances	
$\sigma_0 = [XOH^+_2] - [XO^-] - [XHAsO^-_4] - 2[XAsO^{2-}_4]$ [17]	$\sigma_0 + \sigma_\beta + \sigma_d = 0$ [40]
$\sigma_0 = [XOH^+_2] - [XO^-] - [XHAsO^-_3]$ [18]	$\sigma_0 = [XOH^+_2] + [XOH^+_2\text{–}H_2AsO^-_4] + [XOH^+_2\text{–}HAsO^{2-}_4] + [XOH^+_2\text{–}AsO^{3-}_4] + [XOH^+_2\text{–}Cl^-] - [XO^-] - [XHAsO^-_4] - 2[XAsO^{2-}_4] - [SO^-\text{–}Na^+]$ [41]
	$\sigma_\beta = [XO^-\text{–}Na^+] - [XOH^+_2\text{–}H_2AsO^-_4] - 2[XOH^+_2\text{–}HAsO^{2-}_4] - 3[XOH^+_2\text{–}AsO^{3-}_4] - [XOH^+_2\text{–}Cl^-]$ [42]
	$\sigma_0 = [XOH^+_2] + [XOH^+_2\text{–}H_2AsO^-_3] + [XOH^+_2\text{–}HAsO^{2-}_3] + [XOH^+_2\text{–}Cl^-] - [XO^-] - [XHAsO^-_3] - [SO^-\text{–}Na^+]$ [43]
	$\sigma_\beta = [XO^-\text{–}Na^+] - [XOH^+_2\text{–}H_2AsO^-_3] - 2[XOH^+_2\text{–}HAsO^{2-}_3] - [XOH^+_2\text{–}Cl^-]$ [44]
Surface charge/surface potential relationships	
$\sigma_0 = \frac{CS_AC_p}{F}\psi_o$ [19]	$\sigma_0 = \frac{C_1S_AC_p}{F}(\psi_o - \psi_\beta)$ [45]
	$\sigma_d = \frac{C_2S_AC_p}{F}(\psi_d - \psi_\beta)$ [46]
	$\sigma_d = \frac{S_AC_p}{F}(8\varepsilon_oDRTI)^{1/2}\sinh(F\psi_d/2RT)$ [47]

Note. F is the Faraday constant (C mol_c^{-1}); ψ_o is the surface potential (V); o refers to the surface plane of adsorption; R is the molar gas constant (J mol^{-1} K^{-1}); T is the absolute temperature (K); square brackets represent concentrations (mol L^{-1}); is refers to inner-sphere surface complexation; $[XOH]_T$ is related to the surface site density; N_s, by $[XOH]_T = (S_AC_p10^{18})/N_A * N_s$, where S_A is the surface area (m^2 g^{-1}); C_p is the solid suspension density (g L^{-1}); N_A is Avogadro's number; N_s has units of sites nm^{-2}; σ_0 represents the surface charge (mol_c L^{-1}); C is the capacitance (F m^{-2}); β refers to the plane of outer-sphere adsorption; os refers to outer-sphere surface complexation; C_1 and C_2 are capacitances; d refers to the plane of the diffuse ion swarm; ε_o is the permittivity of vacuum; D is the dielectric constant of water; and I is the ionic strength.

TABLE 2
Modeling Parameters for the Constant Capacitance and Triple-layer Models

Parameter	Constant capacitance model	Triple-layer model
Site density (sites nm^{-2})	2.31	2.31
Capacitance (F m^{-2})	$C = 1.06$	$C_1 = 1.2$ $C_2 = 0.2$
Protonation constant, log K_+(int)	Al oxide = 7.38 Fe oxide = 7.31	Al oxide = 5.0 Fe oxide = 4.3
Dissociation constant, log K_-(int)	Al oxide = −9.09 Fe oxide = −8.80	Al oxide = −11.2 Fe oxide = −9.8
Sodium constant, log K_{Na^+}(int)		Al oxide, 4.0 g L^{-1}, As(III) = −4.45 Fe oxide, 4.0 g L^{-1}, As(V) = −10.6
Chloride constant, log K_{Cl^-}(int)		Al oxide, 4.0 g L^{-1}, As(III) = 6.61 Fe oxide, 4.0 g L^{-1}, As(V) = 10.7
Arsenic constants		
log K_{As}^{1is}(int)	Al oxide, 4.0 g L^{-1}, As(V) = 6.57 Al oxide, 0.5 g L^{-1}, As(V) = 9.39 Fe oxide, 0.5 g L^{-1}, As(V) = 8.16 Fe oxide, 4.0 g L^{-1}, As(III) = 4.52 Fe oxide, 0.5 g L^{-1}, As(III) = 5.47	
log K_{As}^{2is}(int)	Al oxide, 0.5 g L^{-1}, As(V) = 4.11 Fe oxide, 0.5 g L^{-1}, As(V) = 2.63 Fe oxide, 4.0 g L^{-1}, As(III) = −2.70	
log K_{As}^{3is}(int)	Al oxide, 4.0 g L^{-1}, As(V) = −2.95 Al oxide, 0.5 g L^{-1}, As(V) = −3.69 Fe oxide, 0.5 g L^{-1}, As(V) = −2.47	Fe oxide, 4.0 g L^{-1}, As(V) = 5.36
log K_{As}^{1os}(int)		Al oxide, 4.0 g L^{-1}, As(III) = 6.48
log K_{As}^{2os}(int)		Al oxide, 4.0 g L^{-1}, As(III) = 2.84

the variability of log K_+(int) and log K_-(int) was less than the variability of the anion surface complexation constants (26). The capacitance was fixed at $C = 1.06$ F m^{-2} for all materials as in previous constant capacitance modeling of arsenate adsorption on amorphous Al oxide (6, 19). Values of all adjustable parameters, both fixed and optimized, are provided in Table 2.

Triple Layer Modeling

The triple-layer model (27) allows ion adsorption as either inner-sphere or outer-sphere surface complexes. In addition to the inner-sphere surface complexation reactions, Eqs. [1]–[7] in Table 1, the triple-layer model considers outer-sphere surface complexation reactions for the background electrolyte, Eqs. [20] and [21] in Table 1. In the triple-layer model, inner-sphere surface complexation reactions and intrinsic equilibrium constant expressions for arsenate and arsenite are written as for the constant capacitance model, Eqs. [3]–[7] and Eqs. [8]–[14] in Table 1, respectively. The outer-sphere surface complexation reactions for arsenate and arsenite are Eqs. [22]–[28] in Table 1. The intrinsic equilibrium constants for outer-sphere surface complexation are Eqs. [29]–[37] in Table 1. The mass balance for the surface functional group is given by Eq. [38] or Eq. [39] in Table 1. The charge balance expressions are Eq. [40] and either Eqs. [41] and [42] or Eqs. [43] and [44] in Table 1. The relationships between the surface charges and the surface potentials are given by Eqs. [45]–[47] in Table 1.

For the triple-layer application, as for the constant capacitance applications, the surface site density was set at a value of 2.31 sites nm^{-2}, as recommended by Davis and Kent (25) for natural materials. Numerical values for the intrinsic protonation–dissociation constants and surface complexation constants for the background electrolyte were obtained from the literature. For amorphous Fe oxide these constants were log K_+(int) = 4.3, log K_-(int) = −9.8, log K_{Na+}(int) = −9.3, and log K_{Cl-}(int) = 5.4 obtained by Zhang and Sparks (28) for goethite. For amorphous Al oxide these constants were log K_+(int) = 5.0, log K_-(int) = −11.2, log K_{Na+}(int) = −8.6, and log K_{Cl-}(int) = 7.5 obtained by Sprycha (29, 30) for γ-Al_2O_3. Parameter values for crystalline oxides were used since values for amorphous oxides were not available. Arsenic surface complexation constants were fit simultaneously to the adsorption data at three different ionic strengths using either inner-sphere or outer-sphere adsorption mechanisms. For a few systems, it was necessary to optimize log K_{Na+}(int) and log K_{Cl-}(int) after the As surface complexation constants using the FITEQL program. The capacitances were fixed at $C_1 = 1.2$ F m^{-2} and $C_2 = 0.2$ F m^{-2} considered optimum for goethite by Zhang and Sparks (28). Experimentally determined capacitance values using electrokinetic extrapolation range from 1.1 to 1.3 F m^{-2} for C_1 and 0.14 to 0.2 F m^{-2} for C_2 (31). Activity coefficients for the aqueous species were calculated using the Davies equation. Table 2 provides values for all adjustable parameters in the triple-layer model, both fixed and optimized.

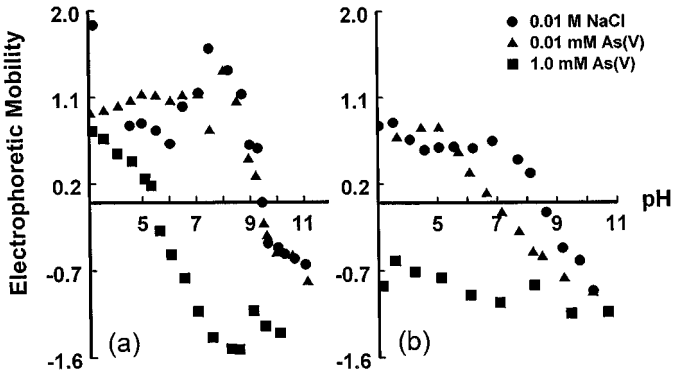

FIG. 1. Electrophoretic mobility of amorphous oxides as a function of pH and total As(V) concentration in 0.01 M NaCl solution: (a) Al oxide, (b) Fe oxide. Circles represent the zero As(V) treatment. Iron oxide data from Suarez *et al.* (15).

RESULTS AND DISCUSSION

Points of Zero Charge

Points of zero charge occurred at pH 9.4 for amorphous Al oxide and pH 8.5 for amorphous Fe oxide (Figs. 1 and 2, Fe oxide data from Suarez *et al.* (15)). Figures 1 and 2 present EM versus pH obtained upon adsorption of arsenate and arsenite, respectively, onto amorphous Al oxide and amorphous Fe oxide. Except for amorphous Al oxide in the presence of As(III) (Fig. 2a), the PZCs are shifted to increasingly lower pH value with increasing As concentration. Shifts in PZC and reversals of EM with increasing ion concentration are characteristics of inner-sphere adsorption. This is clearly seen for amorphous Fe oxide in the presence of As(V) (Fig. 1b). However, lack of shift in PZC cannot be used to infer an outer-sphere adsorption mechanism since inner-sphere surface complex formation is not necessarily accompanied by a change in the mineral surface charge. The PZC of amorphous Al oxide is not shifted in the presence of the lower As(V) concentration (Fig. 1a), thus indicating the formation of either an outer-sphere surface complex or an inner-sphere surface complex that does not change the surface charge. Since the PZC is shifted in the presence of the higher As(V) concentration (Fig. 1a), the formation of an inner-sphere As(V) surface complex on amorphous Al oxide is considered to be more plausible. Identical reasoning would indicate the formation of an inner-sphere surface complex on the surface of amorphous Fe oxide in the presence of As(III) (Fig. 2b). No shift in PZC of amorphous Al oxide was observed in the presence of either concentration of As(III) (Fig. 2a). Therefore these data can be the result of either outer-sphere surface complexation or inner-sphere surface complexation that does not change the surface charge.

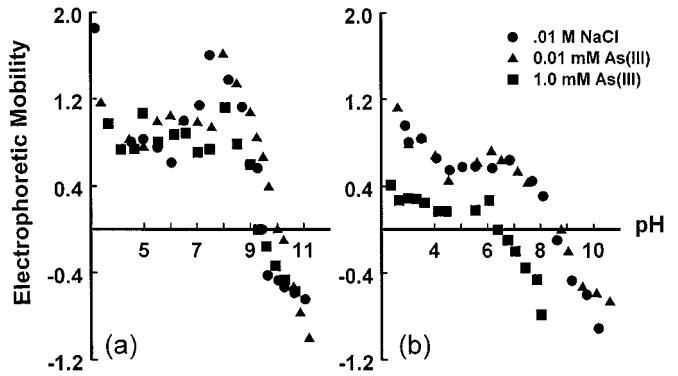

FIG. 2. Electrophoretic mobility of amorphous oxides as a function of pH and total As(III) concentration in 0.01 M NaCl solution: (a) Al oxide, (b) Fe oxide. Circles represent the zero As(III) treatment. Iron oxide data from Suarez *et al.* (15).

Ionic Strength Effects on As Sorption

The effect of ionic strength on As adsorption on amorphous Al and Fe oxides is indicated in Figs. 3–6. Solution ionic strength was varied by two orders of magnitude, from 0.01 to 1.0 M NaCl. Experiments were carried out at two suspension densities of oxide, 0.5 and 4.0 g L^{-1}. Arsenate adsorption on amorphous oxides, as represented in Figs. 3 and 4, decreases with increasing solution pH and exhibits either no ionic strength dependence or increasing adsorption with increasing solution ionic strength. Both of these behaviors are indicative of an inner-sphere adsorption mechanism for arsenate on amorphous Al and Fe oxides, in agreement with the mechanism inferred from PZC shifts of these materials. Arsenite adsorption on amorphous oxides increases with increasing solution pH to an adsorption maximum around pH 8 and decreases with further increases in solution pH (Figs. 5 and 6). Arsenite adsorption on amorphous Al oxide exhibited decreasing adsorption with increasing ionic strength (Fig. 5). This result is indicative of an outer-sphere adsorption mechanism and is not inconsistent with the PZC shift results which could not distinguish between inner- and outer-sphere surface complexation. Arsenite adsorption on amorphous Fe oxide exhibited little

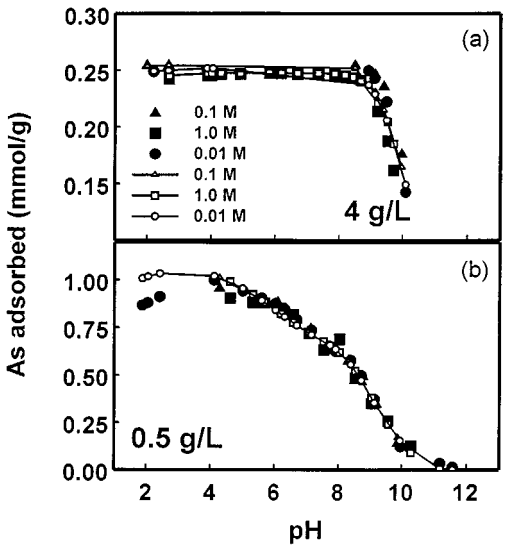

FIG. 3. Fit of the constant capacitance model to As(V) adsorption on amorphous Al oxide as a function of solution pH and ionic strength: (a) solid suspension density = 4.0 g L^{-1}, (b) solid suspension density = 0.5 g L^{-1}. Squares represent experimental data points. Circles represent model fits using inner-sphere As complexes. Model parameters are provided in Table 2.

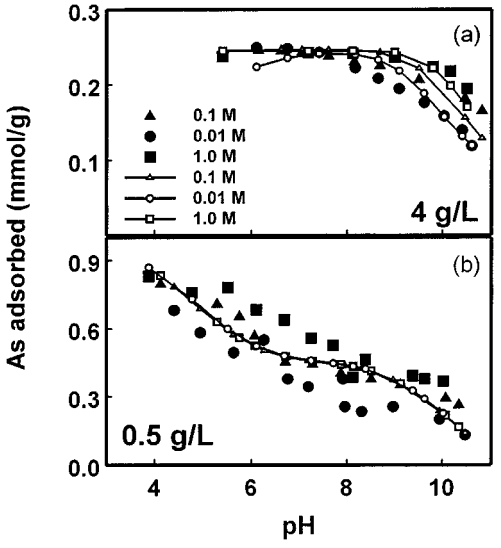

FIG. 4. Fit of surface complexation models to As(V) adsorption on amorphous Fe oxide as a function of solution pH and ionic strength: (a) triple-layer model, solid suspension density = 4.0 g L^{-1}; (b) constant capacitance model, solid suspension density = 0.5 g L^{-1}. Squares represent experimental data points. Circles represent model fits using inner-sphere As complexes. Model parameters are provided in Table 2.

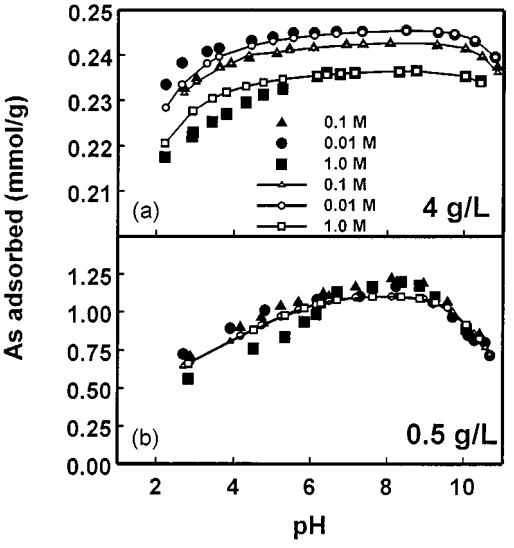

FIG. 6. Fit of the constant capacitance model to arsenite adsorption on amorphous Fe oxide as a function of solution pH and ionic strength: (a) solid suspension density = 4.0 g L^{-1}, (b) solid suspension density = 0.5 g L^{-1}. Squares represent experimental data points. Circles represent model fits using inner-sphere As complexes. Model parameters are provided in Table 2.

ionic strength dependence above pH 6 at a suspension density of 0.5 g L^{-1}, suggestive of an inner-sphere adsorption mechanism (Fig. 6b). Arsenite adsorption on amorphous Fe oxide at a suspension density of 4 g L^{-1} (Fig. 6a) and below pH 6 at a suspension density of 0.5 g L^{-1} decreased with increasing ionic strength, suggesting an outer-sphere adsorption mechanism (Fig. 6b). These results are in agreement with the PZC shift data which also suggest the possibility of both inner- and outer-sphere As(III) surface complexes on amorphous Fe oxide.

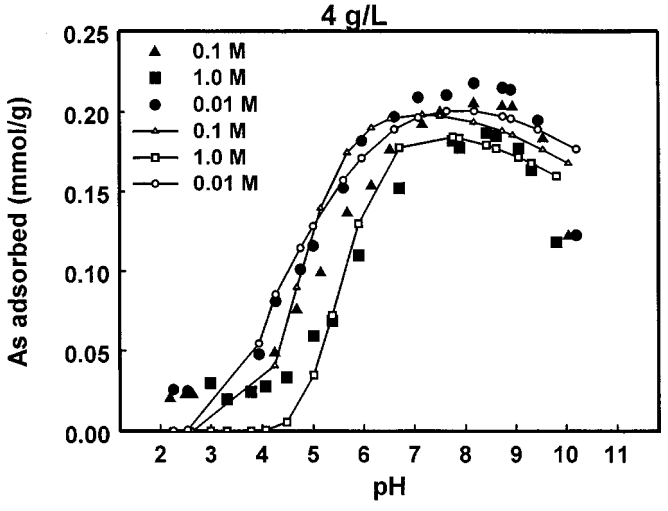

FIG. 5. Fit of triple-layer model to arsenite adsorption on amorphous Al oxide as a function of solution pH and ionic strength. Solid suspension density = 4.0 g L^{-1}. Squares represent experimental data points. Circles represent model fits using outer-sphere As complexes. Model parameters are provided in Table 2.

Spectroscopic Results

Aqueous solution spectra of As(III). The positions and relative intensities of the Raman- and infrared (IR)-active bands of As(III) are sensitive to changes in solution pH as shown in Fig. 7 and Table 3. At pH 10.5, the dominant solution species is $AsO(OH)_2^-$ and the Raman spectrum is characterized by two

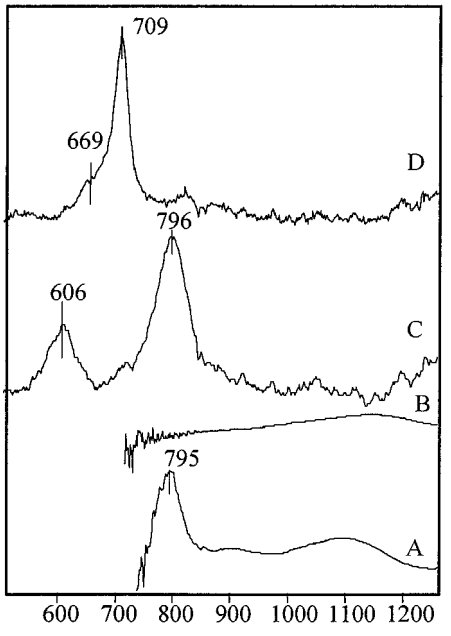

FIG. 7. Raman and ATR-FTIR spectra of a 0.1 M As(III) solution: ATR-FTIR spectra were obtained at pH 10.5 (A) and pH 5 (B). Similarly, Raman spectra are shown at pH 10.5 (C) and pH 5 (D).

TABLE 3
Raman and IR Band Positions and Assignments of As(III) and As(V) Species in Aqueous Solution

Oxidation state	Species	This study Raman		This study IR		Lit Raman		Assignment	Description	Ref.
As(III) at pH 5	$As(OH)_3$							Symmetry C_{3v}		
		669	(vw, $P = 0.5$)		bc*	655		ν_3 (E)	As–OH stretch	(31, 32)
		709	(s, $P = 0.01$)		bc*	710		ν_1 (Al)	Symm As–OH stretch	(31, 32)
				795					As–O stretch	(31, 32)
As(III) at pH 10.5	$AsO(OH_2)^-$							Symmetry $C_s(4A' + 2A'')$		
						320		$\nu3$, $\nu4$, & $\nu6$		(31)
						370		$\nu3$, $\nu4$, & $\nu6$		(31)
						570		$\nu2(A')$	Symm stretch As–(OH)	(31)
		606	($P = 0.49$)			610		$\nu5(A'')$	Asymm stretch As–(OH)	(31)
		796	($P = 0.15$)			790		$\nu1(A')$	As–O stretch	(31)
As(V) at pH 5	$AsO_2(OH)_2^-$							Symmetry C_{2v}		
						285		a1	Bend (OH)–As–(OH)	(33)
		319				315		a2	Torsion O–As–O	(33)
		385				365		a1, b1, b2	Bend O–As–O	(33)
		742	($P = 0.19$)			745		a1	Symm stretch As–OH	(33)
						765		b2	Asymm Stretch As–OH	(33)
						843			Polymeric vibration	(33)
		874	($P = 0.15$)	878		875	875	a1	Symm stretch As–O	(33)
				907		915	908	b1	Asymm stretch As–O	(33)
As(V) at pH 9	$AsO_3(OH)^{2-}$							Symmetry C_{3v}		
		327				327		a1	Symm bend As–O	(33)
		394				380		e	Asymm bend As–O	(33)
		700	($P = 0.13$)			707		a1	Symm stretch As–OH	(33)
						811			Polymeric vibration	(33)
		834	($P = 0.27$)			838		a1	Symm stretch As–O	(33)
				858		866	860	e	Asymm stretch As–O	(33)

bands at 606 and 796 cm^{-1}. The low-frequency cutoff of the ZnSe ATR-FTIR cell used in this study was 750 cm^{-1}. Consequently, it was not possible to detect the IR-active vibrations of arsenite <750 cm^{-1}. One of the advantages of Raman spectroscopy is that this frequency limitation is not present. The Raman-active bands in the 400 to 750 cm^{-1} region are readily observed. The positions of the Raman-active bands are in good agreement with an earlier Raman study of arsenious acid and arsenites in aqueous solution (29). The 606 cm^{-1} band was assigned by Loehr and Plane (32) to an asymmetric stretching vibration of As–OH groups and the 796 cm^{-1} band was assigned to the stretching vibration of the As–O bond. The As–O is a shorter, stronger bond compared to that of the As–OH groups; consequently, the position of the υ(As–O) vibration(s) occurs at higher frequencies relative to their υ(As–OH) counterparts. These assignments are also supported by a recent theoretical study of the arsenite system (33).

Upon lowering the pH to 5, the dominant species in aqueous solution is $As(OH)_3$ and the Raman spectrum is characterized by a strong band at 709 cm^{-1}. In addition, a weak shoulder appears at 669 cm^{-1}. The 709 cm^{-1} band is assigned to the symmetric stretching vibration of the As–OH groups. The symmetry of the neutral monomer $As(OH)_3$ has a high symmetry of C_{3v}, which is consistent with the measured Raman depolarization ratio of this band of 0.01, which was the most strongly polarized Raman band measured for any of the aqueous arsenate or arsenite species (Fig. 8 and Table 3). As shown in Fig. 8, the intensity of the totally symmetric vibration at 709 cm^{-1} is completely extinguished from the perpendicular Raman spectrum at pH 5. For highly symmetric vibrations, the Raman depolarization ratio tends toward zero, which can be used to identify the symmetry of molecular vibrations (22). The small depolarization ratio confirms the assignment of the 709 cm^{-1} band to symmetric As–OH stretch and is supported by the study of Tossell (33) who used GAUSSIAN94 to predict Raman intensities and depolarization ratios.

The position of the υ(As–OH) bands at pH 10.5 occurs at 606 cm^{-1}. Upon lowering the pH to 5, two bands occur at 669 and 709 cm^{-1} and indicate that the As–OH bond becomes shorter and stronger upon lowering the pH. These results are supported by the recent theoretical study of Tossell (33). Using computational methods, he observed that the bond length decreased and the positions of the calculated υ(As–O) or υ(As–OH) bands increased upon protonation of the hydrated As(III) complexes going from $AsO_2(OH)^{-2}$ to $AsO(OH)_2^-$. These theoretical results support the experimental findings showing that the frequency for both the υ(As–OH) and υ(As–O) vibrations of As(III) complexes shift to higher values upon lowering the pH.

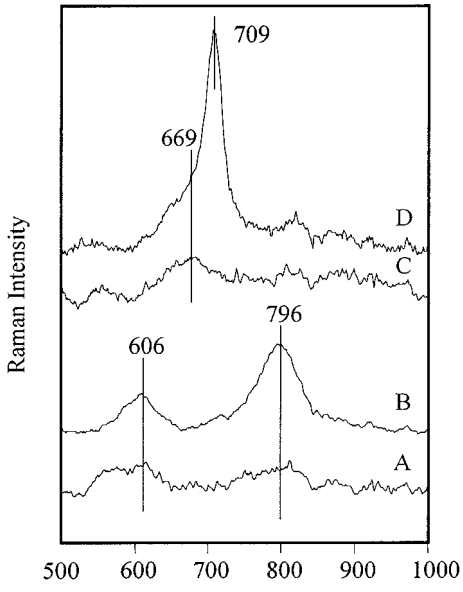

FIG. 8. Polarized Raman spectra of a 0.1 M As(III) solution at pH 10.5 and pH 5: (A) perpendicular polarization at pH 10.5, (B) parallel polarization at pH 10.5, (C) perpendicular polarization at pH 5, (D) parallel polarization at pH 5.

Aqueous solution spectra of As(V). Raman and IR spectra of a 0.1 M aqueous solution of 0.1 M As(V) are shown in Fig. 9 at pH values of 5 and 9, corresponding to the $AsO_2(OH)_2^-$ and $AsO_3(OH)^{-2}$ species, respectively. The observed band positions and depolarization ratios are compared to literature values along with band assignments in Table 3. As shown, the positions and relative intensities of the bands in both the Raman and IR spectra of the arsenate solutions are strongly affected by changes in pH. At pH 5, the predominant As(V) species in solution is $AsO_2(OH)_2^-$ with a symmetry of C_{2v}. The two predominant bands in the Raman spectra occur at 742 and 874 cm^{-1} and have been assigned to v(As–OH) and v(As–O) vibrations, respectively. The positions of the v(As–O) bands in the IR spectrum occur at 878 and 907 cm^{-1}, which have been assigned (34) as the symmetric and asymmetric stretching modes of the two equivalent As–O bonds (Table 3). These results are similar to the FTIR results of Suarez *et al.* (15) for As(V) adsorption on amorphous Al oxide. Although Raman-active, the intensity of the 907 cm^{-1} band is weak with an assigned symmetry of b_1. The low-frequency cutoff of the ZnSe ATR cell used in this study was 750 cm^{-1} so it was not possible to observed the IR-active arsenate bands in aqueous solutions with frequencies <750 cm^{-1}. Upon increasing the pH to 9, the predominant solutions species becomes $AsO_3(OH)^{-2}$ with symmetry of C_{3v}. The two dominant bands in the Raman spectra are shifted to 700 and 834 cm^{-1}, respectively, and correspond to the v(As–OH) and to the symmetric v(As–O) modes. The corresponding IR spectrum is characterized by a strong band 858 cm^{-1} assigned by Vansant *et al.* (34) as the asymmetric v(As–OH) mode with a symmetry E under the C_{3v} point group.

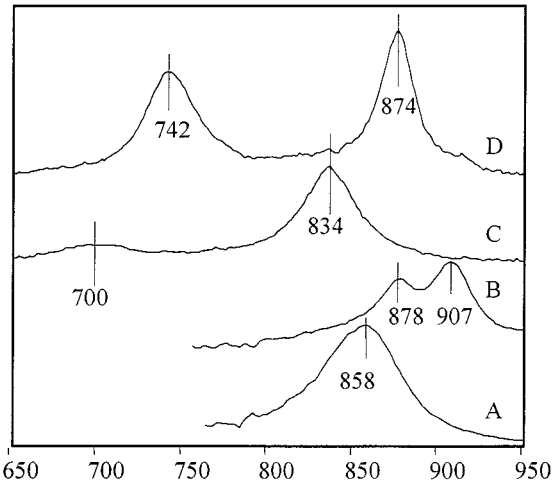

FIG. 9. Raman and ATR-FTIR spectra of a 0.1 M As(V) solution: ATR-FTIR spectra are shown at pH 9 (A) and pH 5 (B). Similarly, Raman spectra are shown at pH 9 (C) and pH 5 (D).

In an earlier Raman study of arsenic acid $AsO(OH)_3$ and its anions in aqueous solution, Vansant *et al.* (34) assigned the 700 cm^{-1} band at high pH and the bands at 745 and 765 cm^{-1} at pH 5 to the stretching motion of As–(OH) groups. Examination of the original spectra reported by Vansant *et al.* (34) showed that the positions of the 745 cm^{-1} and 765 cm^{-1} bands were determined using a curve-fitting approach. In the original data, however, only one band centered at approximately 750 cm^{-1} is apparent in agreement with the results presented here (Fig. 9). Although splitting of the v(As–OH) modes is expected based on group theory, the v(As–OH) modes are nearly degenerate.

Upon lowering the pH of the aqueous solutions from 9 to 5, the positions of both the IR- and Raman-active As–O and As–OH stretching bands increase in frequency (Fig. 9) similar to the As(III) system. The pH-induced shifts of the As–O stretching band are consistent with a recent IR study of phosphate in aqueous solution and bound to an Fe oxide surface (35). Normal mode analysis of the vibrational spectra of solutions containing the chemical species PO_4^{-3}, HPO_4^{-2}, $H_2PO_4^-$, and H_3PO_4 showed a significant increase in the force constant for the P–O and P–OH bands with increasing protonation based upon a normal mode analysis of the vibrational spectra (35). In other words, the P–O bond becomes stronger upon lowering the pH and is reflected in the IR and Raman spectra by a shift of the v(PO) bands to higher energy.

To test this hypothesis, the semiempirical molecular orbital package MOPAC (Version 5.0) was used to calculate the structure, determine the force constants, and predict the vibrational spectra of the AsO_4^{-3}, $AsO_3(OH)^{-2}$, $AsO_2(OH)_2^-$, and $AsO(OH)_3$ species. MOPAC is a general-purpose semiempirical molecular orbital package for the study of chemical structures and reactions. Using the PM3 basis set, the geometries of the AsO_4^{-3}, $AsO_3(OH)_2^-$, $AsO_2(OH)_2^-$, and $AsO(OH)_3$ species were optimized. Based on these structures, the MOPAC model was used to calculate the force constants for the As–O and

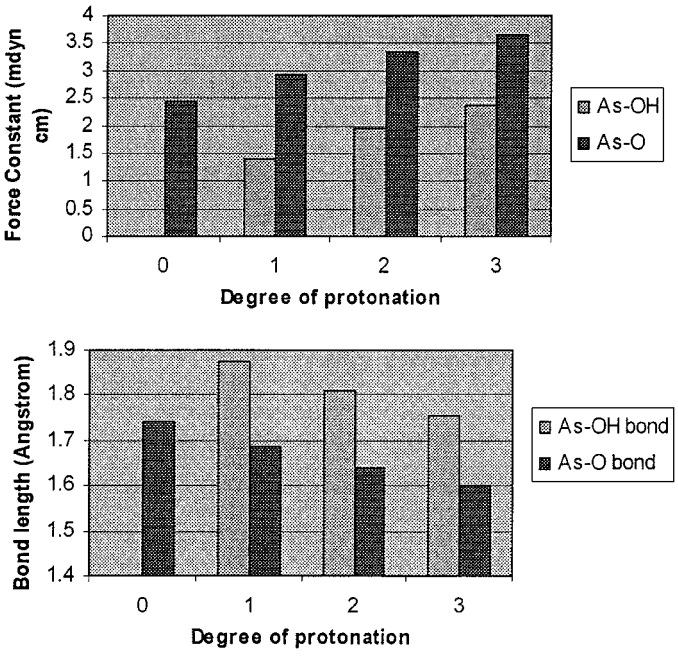

FIG. 10. Calculated force constants and bond lengths for the As–O and As–OH bonds, As(V), obtained using the semiempirical molecular orbital package MOPAC and the PM3 basis set.

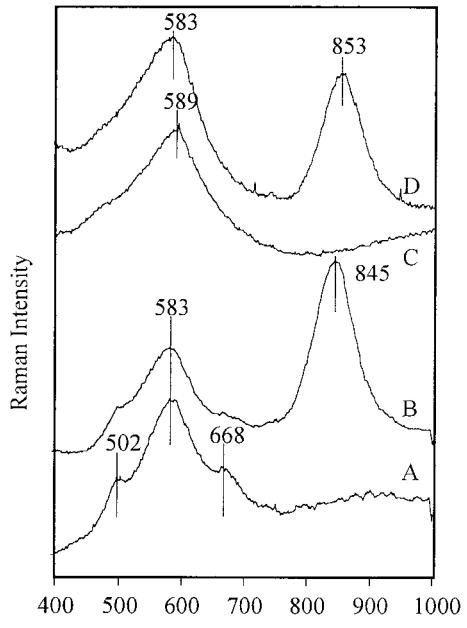

FIG. 11. Raman spectra of an aqueous suspension of amorphous Al oxide with and without As(V). Raman spectrum of the aqueous amorphous Al oxide suspension at pH 9 (A), same conditions with As(V) sorbed (B), aqueous amorphous Al oxide suspension at pH 5 (C), and aqueous amorphous Al oxide at pH 5 with As(V) sorbed (D).

As–(OH) bonds. Using this model, the force constants for the As–O and As–OH bonds were calculated and the results are shown in Fig. 10. The force constant of a chemical bond is a measure of how strong the chemical bond is. As the degree of protonation increased (i.e., $AsO_4^{-3} \rightarrow AsO_3(OH)^{-2} \rightarrow AsO_2(OH)_2^{-} \rightarrow AsO(OH)_3$) the force constants for both the As–O and As–OH bonds increased, indicating that the As–O and As–OH bonds are stronger at lower pH. These results are in good agreement with the pH-induced increase of the υ(As–O) and υ(As–OH) bands upon lowering the pH. These data also agree with the experimental data of Persson *et al.* (35) for the phosphate system.

As(V) sorption to Al oxide. Raman spectra of arsenate sorbed to amorphous Al oxide at pH 5 and 9 are shown in Fig. 11. The presence of sorbed arsenate is clearly resolved by the strong υ(As–O) band at 853 and 845 cm^{-1} at pH values of 5 and 9, respectively. Upon lowering the pH from 9 to 5, the position of the υ(As–O) band increases by 8 cm^{-1}. The positions of the υ(As–O) band in aqueous solution samples are 834 cm^{-1} at pH 9 and 874 cm^{-1} at pH 5. Thus, the frequency of the υ(As–O) band of sorbed arsenate is intermediate to the positions observed in aqueous solution at pH values of 5 and 9. Furthermore, a much smaller increase in frequency for the υ(As–O) band of sorbed arsenate is observed compared to the 40 cm^{-1} blue-shift that occurs in aqueous solution.

IR spectra of arsenate sorbed to the Al oxide samples at pH 5 and 9 are shown in Fig. 12. Similar to the Raman results, the presence of arsenate is clearly resolved by a band in the 856 to 866 cm^{-1} region. The IR spectra of the Al oxide itself has IR-active bands at 949 cm^{-1}, corresponding to bending vibrations of Al–O–H groups. In addition, carbonate is present in this sample as revealed by the carbonate bands at 1070 cm^{-1} consistent with the high pH of the sample. Difference spectra were obtained by subtracting the Al oxide spectrum from the spectrum

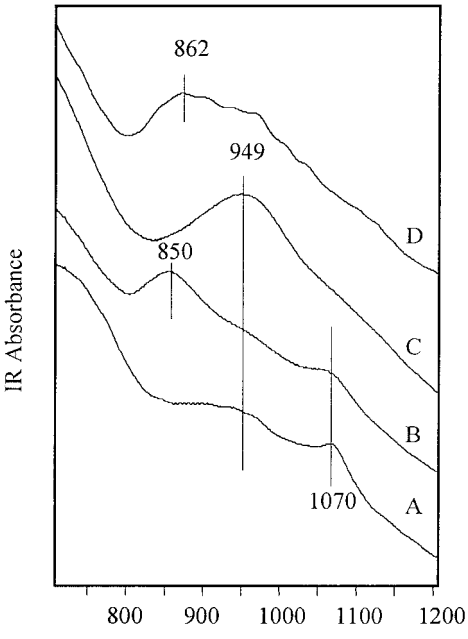

FIG. 12. KBr pellet IR spectra of Al oxide at pH 9 (A), Al oxide with sorbed As(V) at pH 9 (B), Al oxide at pH 5 (C), and Al oxide with sorbed As(V) at pH 5 (D).

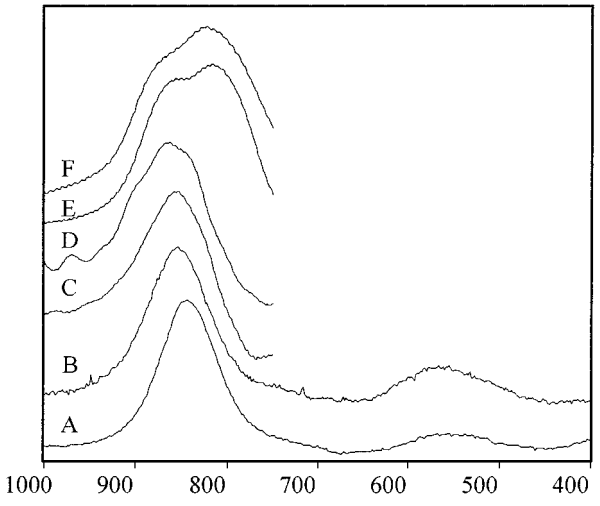

FIG. 13. Difference spectra of As(V) sorbed to amorphous Al and Fe oxides. Raman difference spectrum of As(V) sorbed to Al oxide (A) with the spectrum of the Al oxide subtracted at pH 9, (B) same as (A) but at pH 5, (C) KBr pellet IR difference spectrum of As(V) sorbed to Al oxide with the IR spectrum of the Al oxide subtracted at pH 9, (D) same as (C) but at pH 5, (E) KBr pellet IR difference spectrum of As(V) sorbed to Fe oxide with the IR spectrum of the Fe oxide subtracted at pH 9, (F) same as (E) but at pH 5.

of the arsenate–Al oxide sample at pH 5 and 9 and the difference spectra are shown in Fig. 13. For comparison, difference Raman spectra of arsenate sorbed to Al oxide and difference IR spectra of arsenate sorbed to Fe oxide are included in Fig. 13. The Raman and IR spectra of arsenate sorbed to Al oxide are very similar. In both the Raman and the IR spectra, the position of the υ(As–O) band increases in frequency upon decreasing the pH from 9 to 5 by about 10 cm^{-1}. Based on the behavior of arsenate in aqueous solution, this results indicates that the As–O bond strengthens upon lowering the pH.

In aqueous solution at pH 5, the υ(As–O) band is split into two components corresponding to the symmetric and asymmetric υ(As–O) vibrational modes. No splitting is evident in the IR spectrum as arsenate sorbed to Al oxide at pH 9 (Fig. 13C) and some minor splitting is evident at pH 5 (Fig. 13D). In general, the spectra of arsenate sorbed to the Al oxide are very different from those of arsenate in solution. This difference and the lack of pH dependence on the positions of the υ(As–O) modes indicate that these modes are "protected" from changes in pH and indicate that these groups are involved in direct complexation to the surface. Based on the similarity of both the Raman and the IR spectra at pH 5 and 9, the data suggest that a similar sorption mechanism occurs over this pH range. These results are consistent with the formation of an inner-sphere complex at both pH values. At the present time, it is not clear based on the spectroscopic data if one or both of the (As–O) groups in the $AsO_2(OH)_2^-$ complex are involved in surface complexation.

In aqueous solution, the positions of the IR- and Raman-active υ(As–O) bands are separated by 24 and 31 cm^{-1}, respectively. These separations are greatly diminished for arsenate sorbed to the Al oxide surface, indicating that the surface has effectively lowered the symmetry of the sorbed arsenate species from C_{3v} in solution to a complex with lower symmetry. The IR spectrum of a poorly crystalline Al–arsenate sample has a broad, poorly resolved band at 887 cm^{-1} and a well-resolved band at 745 cm^{-1} (36). The IR- and Raman-active υ(As–O) bands in the 844–865 cm^{-1} region are assigned to the υ(As–O) vibration of an inner-sphere Al–O–As complex.

As(V) sorption to Fe oxide. IR spectra of arsenate sorbed to the amorphous Fe oxide sample at pH 5 and 9 are shown in Fig. 14. Unlike the Al oxide system where a single band in the 850–862 cm^{-1} region was observed, the spectra clearly reveal two bands at 817 and 854 cm^{-1} at pH 9 (Fig. 13E) and 824 and 861 cm^{-1} at pH 5 (Fig. 13F), respectively. These results are similar to the FTIR results of Suarez *et al.* (15) for As(V) adsorption on amorphous Fe oxide. The positions of the 817 cm^{-1} (pH 9) and 824 cm^{-1} (pH 5) bands are too high in frequency to be assigned to an υ(As–OH) vibration. The spectra of arsenate sorbed to Fe oxide are very distinct from the spectra of arsenate sorbed to the Al oxide surface. These differences are shown clearly in the difference IR and Raman spectra plotted in Fig. 13. In contrast to the single υ(As–O) band observed for arsenate sorbed to amorphous Al oxide, the sorbed species is characterized by two bands for arsenate sorbed to Fe oxide. In an earlier IR study of arsenate sorbed to goethite (37), a similar band at 834 cm^{-1} was reported that was assigned to the υ(As–OH) of As–O–Fe groups. This assignment is supported by a more recent Raman and IR study of several metal-containing arsenate salts by Myneni *et al.* (36). In the case of As(V)/Fe oxide complex, two bands are observed with a separation of about 40 cm^{-1}. The "splitting" of the υ(As–O) vibration can

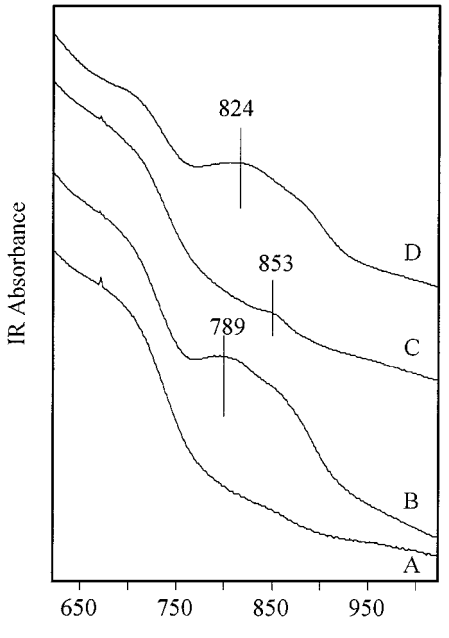

FIG. 14. KBr pellet IR spectra of Fe oxide at pH 9 (A), Fe oxide with sorbed As(V) at pH 9 (B), Fe oxide at pH 5 (C), and Fe oxide with sorbed As(V) at pH 5 (D).

be explained in two ways. First, the two vibrations correspond to the symmetric and asymmetric stretching modes of a sorbed $AsO_2(OH)_2^-$ complex. The separation between the symmetric and asymmetric vibrations, however, is larger than the splitting in aqueous solution. Furthermore, in aqueous solution the asymmetric v(As–OH) vibration (high-frequency band) is observed to have more intensity than the symmetric v(As–OH) vibration. The opposite behavior is observed here. The second interpretation of the spectral data is that there are two distinct types of As–O groups. The 817–824 cm^{-1} band would be assigned the Fe–O–As groups and the 854–861 cm^{-1} band would correspond to non-surface-complexed As–O bonds of the adsorbed As(V) species. Suarez *et al.* (15) previously proposed a surface species of $HAsO_4^-$ on amorphous Al oxide, consistent with their FTIR, PZC, and titration results.

The spectral results are consistent with the sorption data. The IR and Raman spectra of As(V) sorbed to Fe and Al oxide samples are distinct from IR and Raman spectra of Fe and Al arsenate salts (36), which indicates that As(V) is bound as a surface complex and not as a precipitated solid phase. As shown in Figs. 3 and 4, arsenate sorption on the Fe and Al oxide samples are distinct in two ways. First, less arsenate is sorbed to the Fe oxide surface. Second, sorption of arsenate on Fe oxide is strongly influenced by changes in ionic strength, whereas sorption of arsenate on the Al oxide surface was not greatly influenced by changes in ionic strength.

As(III) sorption to Fe and Al oxides. In contrast to the spectra of arsenate sorbed to Fe and Al oxides, it was difficult to detect the presence of sorbed arsenite at pH 5 or 10.5 on the surface of either Fe oxide or Al oxide. In the case of arsenite sorption on Fe at pH 5, the As(III) species is clearly identified by the band at 783 cm^{-1} that corresponds to the As–O vibration. These results are in reasonable agreement with the earlier study of As(III) sorption to Fe and Al oxides by Suarez *et al.* (15) who reported bands at 794 and 631 cm^{-1}. At pH 10.5 the IR spectra (Fig. 15) of treated and untreated samples are significantly altered compared with the spectra at pH 5. This would indicate that the sample was partially transformed under the high pH conditions. The fact that no bands (IR or Raman) are observed in the 750–800 cm^{-1} region in solution at pH 5 (Fig. 7) would suggest that the 783 cm^{-1} may result from the formation of an inner-sphere surface complex. The Fe oxide of substrate had a very intense IR band in the 600 cm^{-1} region which precluded observation of the band(s) in the 600–630 cm^{-1} region. In the case of As(III) sorption to aluminum oxide, no discernible features were observed that could be attributed to an As(III) surface complex. Based on these results, the spectral methods used here are not as well-suited to observe more weakly held surface complexes that do not involve direct coordination of the As(III) complex to the surface through a As–O–X bond.

Modeling Results

The ability of the constant capacitance model to describe arsenate adsorption on amorphous Al oxide is depicted in Fig. 3.

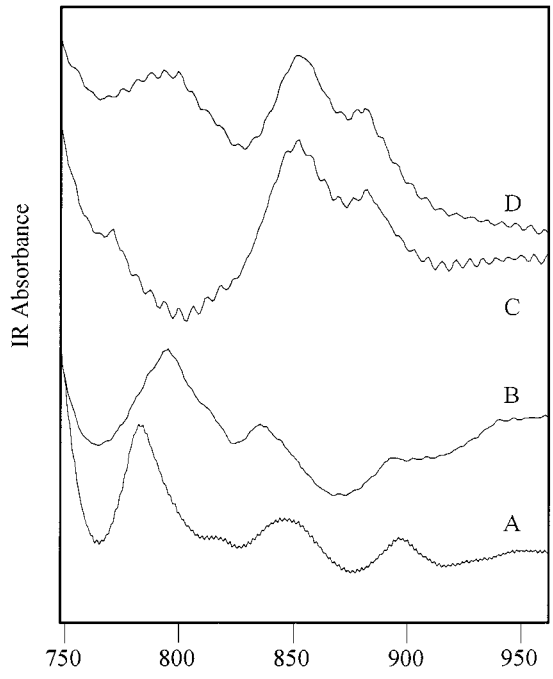

FIG. 15. KBr pellet FTIR spectra of Fe oxide at pH 10.5 (A). (B) Same as (A) but with the addition of As(III). (C) Fe oxide at pH 5. (D) Same as (C) but with the addition of As(III).

With the exception of three data points near pH 2 for the lower solid suspension density (Fig. 3b), the model describes the data quantitatively. Judging from the good fit, the inner-sphere adsorption mechanism assumed in the model is appropriate and is consistent with the PZC shift, ionic strength dependence, and spectroscopic results.

Figure 4 shows surface complexation model fits to arsenate adsorption on amorphous Fe oxide. Since the data exhibited some ionic strength dependence, the triple-layer model, which explicitly accounts for changes in adsorption with changing solution ionic strength, was evaluated for its ability to describe the data. At the higher solid suspension density (Fig. 4a) the triple-layer model was able provide some ionic strength dependence in its description of arsenate adsorption as an inner-sphere surface complex. To obtain ionic strength-dependent fits, it was necessary to also optimize the intrinsic surface complexation constants for adsorption of Na^+ and Cl^- from the background electrolyte. Triple-layer fitting of the arsenate adsorption data at the lower solid suspension density provided a lower quality fit. Therefore, the fit shown in Fig. 4b is the result of constant capacitance modeling. While the fit to the data overall is good, the constant capacitance model is by definition unable to describe changes in adsorption with changes in solution ionic strength. The inner-sphere adsorption mechanism for arsenate adsorption used in the modeling is in agreement with the PZC shift and ionic strength dependence results.

Arsenite adsorption on amorphous Al oxide (Fig. 5) was found to decrease significantly with increasing solution ionic strength and was therefore described with the triple-layer model and an

outer-sphere As(III) surface configuration. Adequate descriptions of the adsorption curves were obtained solely for two bidentate outer-sphere surface complexes formed in the reactions given by Eqs. [27] and [28] and described by the surface complexation constants Eqs. [36] and [37]. It was necessary to also optimize the intrinsic surface complexation constants for adsorption of Na^+ and Cl^- from the background electrolyte. Using an outer-sphere adsorption mechanism for arsenite, the triple-layer model can describe the trends in adsorption occurring with changes in solution ionic strength (Fig. 5). The outer-sphere adsorption mechanism used in the modeling is consistent with the ionic strength dependence and spectroscopic results.

The ability of the constant capacitance model to describe arsenite adsorption on amorphous Fe oxide is indicated in Fig. 6. The data show some ionic strength dependence, suggesting the need for the triple-layer model. However, the triple-layer model, despite being able to provide some ionic strength dependence, gave an overall worse fit than the constant capacitance model. For this reason the constant capacitance model was chosen. For the higher solid suspension density (Fig. 6a), the constant capacitance model describes the change in adsorption as a function of solution ionic strength and fits the data quantitatively, except at low pH. This result is surprising since this model assumes an inner-sphere adsorption mechanism and is not expected to describe the effect of ionic strength changes on adsorption. For the lower solid suspension density (Fig. 6b), the constant capacitance model fits the data well but is unable to describe the reduced adsorption occurring at high ionic strength below pH 6.

CONCLUSIONS

The results of all experimental methods both macroscopic (PZC shifts and ionic strength effects) and microscopic (Raman and FTIR spectroscopies) provide self-consistent mechanisms for As adsorption on amorphous oxides. Arsenate forms inner-sphere surface complexes on both amorphous Al and Fe oxides. Arsenite forms both inner-and outer-sphere surface complexes on amorphous Fe oxide and outer-sphere surface complexes on amorphous Al oxide.

ACKNOWLEDGMENTS

Gratitude is expressed to Mr. H. Forster, Mr. P. Parker, and Ms. M. Scott for technical assistance.

REFERENCES

1. Masscheleyn, P. H., Delaune, R. D., and Patrick, W. H., *Environ. Sci. Technol.* **25,** 1414 (1991).
2. Nickson, R., McArthur, J., Burgess, W., Ahmed, K. M., Ravenscroft, P., and Rahman, M., *Nature* **395,** 338 (1998).
3. Anderson, M. A., Ferguson, J. F., and Gavis, J., *J. Colloid Interface Sci.* **54,** 391 (1976).
4. Pierce, M. L., and Moore, C. B., *Water Res.* **16,** 1247 (1982).
5. Hsia, T.-H., Lo, S.-L., Lin, C.-F., and Lee, D.-Y., *Colloids Surf. A: Physicochem. Eng. Aspects* **85,** 1 (1994).
6. Manning, B. A., and Goldberg, S., *Environ. Sci. Technol.* **31,** 2005 (1997).
7. Pierce, M. L., and Moore, C. B., *Environ. Sci. Technol.* **14,** 214 (1980).
8. Waychunas, G. A., Rea, B. A., Fuller, C. C., and Davis, J. A., *Geochim. Cosmochim. Acta* **57,** 2251 (1993).
9. Fuller, C. C., Davis, J. A., and Waychunas, G. A., *Geochim. Cosmochim. Acta* **57,** 2271 (1993).
10. Hsia, T. H., Lo, S. L., and Lin, C. F., *Chemosphere* **25,** 1825 (1992).
11. Hering, J. G., Chen, P.-Y., Wilkie, J. A., Elimelich, M., and Liang, S., *J. Am. Water Works. Assoc.* **88,** 155 (1996).
12. Wilkie, J. A., and Hering, J. G., *Colloids Surf. A: Physicochem. Eng. Aspects* **107,** 97 (1996).
13. Raven, K. P., Jain, A., and Loeppert, R. H., *Environ. Sci. Technol.* **32,** 344 (1998).
14. Jain, A., Raven, K. P., and Loeppert, R. H., *Environ. Sci. Technol.* **33,** 1179 (1999).
15. Suarez, D. L., Goldberg, S., and Su, C., *Am. Chem. Soc. Symp. Ser.* **715,** 136 (1998).
16. Fendorf, S., Eick, M. J., Grossl, P., and Sparks, D. L., *Environ. Sci. Technol.* **31,** 315 (1997).
17. Manning, B. A., Fendorf, S. E., and Goldberg, S., *Environ. Sci. Technol.* **32,** 2383 (1998).
18. McBride, M. B., *Clays Clay Miner.* **45,** 598 (1997).
19. Goldberg, S., *Soil Sci. Soc. Am. J.* **50,** 1154 (1986).
20. Dzombak, D. A., and Morel, F. M. M., "Surface Complexation Modeling: Hydrous Ferric Oxide." Wiley & Sons, New York, 1990.
21. Sims, J. T., and Bingham, F. T., *Soil Sci. Soc. Am. Proc.* **32,** 364 (1968).
22. Long, D. A., "Raman Spectroscopy." McGraw–Hill, New York, 1977.
23. Stumm, W., Kummert, R., and Sigg, L., *Croat. Chem. Acta* **53,** 291 (1980).
24. Herbelin, A. L., and Westall, J. C., "FITEQL: A Computer Program for Determination of Chemical Equilibrium Constants from Experimental Data." Rep. 94-01, Version 3.1, Dept. of Chemistry, Oregon State Univ., Corvallis, 1994.
25. Davis, J. A., and Kent, D. B., *Rev. Mineral.* **23,** 117 (1990).
26. Goldberg, S., and Sposito, G., *Soil Sci. Soc. Am. J.* **48,** 772 (1984).
27. Davis, J. A., James, R. O., and Leckie, J. O., *J. Colloid Interface Sci.* **63,** 480 (1978).
28. Zhang, P., and Sparks, D. L., *Environ. Sci. Technol.* **24,** 1848 (1990).
29. Sprycha, R., *J. Colloid Interface Sci.* **127,** 1 (1989).
30. Sprycha, R., *J. Colloid Interface Sci.* **127,** 12 (1989).
31. Sprycha, R., *J. Colloid Interface Sci.* **102,** 173 (1984).
32. Loehr, T. M., and Plane, R. A., *Inorg. Chem.* **7,** 1708 (1968).
33. Tossell, J. A., *Geochim. Cosmochim. Acta* **61,** 1613 (1997).
34. Vansant, F. K., van der Veken, B. J., and Desseyn, H. O., *J. Mol. Struct.* **15,** 425 (1972).
35. Persson, P., Nilsson, N., and Sjoberg, S., *J. Colloid Interface Sci.* **177,** 263 (1996).
36. Myneni, S. C. B., Traina, S. J., Waychunas, G. A., and Logan, T. J., *Geochim. Cosmochim. Acta* **62,** 3285 (1998).
37. Lumsdon, D. G., Fraser, A. R., Russell, J. D., and Livesey, N. T., *J. Soil Sci.* **35,** 381 (1984).